# Compact FEL-Driven Inverse Compton Scattering Gamma-Ray and UV Source

M. Placidi [a], S. Di Mitri [b], C. Pellegrini [c,d] and G. Penn [a]

[a] Lawrence Berkeley National Laboratory, Berkeley, California 94720, USA

[b] Elettra - Sincrotrone Trieste S.C.p.A., 34149 Basovizza, Trieste, Italy

[c] SLAC National Accelerator Laboratory, Menlo Park, California 94025, USA

[d] University of California, Los Angeles, California 90095, USA

## Abstract

Many research and applications areas require photon sources capable of producing Gamma-ray beams in the multi-MeV energy range with reasonably high fluxes and compact footprints. Besides industrial, nuclear physics and defense applications, a considerable interest comes from the possibility to assess the state of conservation of cultural assets like statues, columns etc. via visualization and analysis techniques using high energy photon beams. Computed Tomography scans presently provide high quality three-dimensional imaging in industry, museums and medical diagnostics. We propose an innovative scheme based on Inverse Compton Scattering of a high intensity ultra-violet (UV) beam generated in a free-electron laser (FEL) by the primary electron beam. The novel scheme can produce quasi-monochromatic UV radiation in the 15–20 eV range, and gamma-rays in the 10-20 MeV range.

## 1. Introduction

Compact tunable X-rays sources associated with various imaging techniques have been developed and used in a large number of areas ranging from spectroscopy, radiology, medical and biological applications to security, aerospace industry and cultural heritage science. In particular the field of applications in Geo-archaeology is very wide. It goes from very small archaeological findings like prehistoric teeth and old jewelry, to large artifacts and burial objects wrapped inside soil blocks*, possibly involving considerable sizes. Depending on the nature and composition of the artifacts inside the soil blocks their tomographic analysis may require very penetrating and high power sources of X-rays [1–5] in combination with detectors capable of providing good resolution imaging for this type of radiation. Methods of X-ray production presently include Inverse Compton Scattering (ICS) facilities [6] and synchrotron radiation sources from insertion devices in electron storage rings. Contrast imaging of massive sculptures would profit [7] from radiation sources more powerful than the X-ray CT industrial instruments operating in the 450 keV range.

We discuss the feasibility and the performance of an ICS-based scheme where the electron beam interacts with its own radiation emitted in a Free Electron Laser (FEL). The energy of the outgoing radiation has a steeper dependence on the electron energy than a classical ICS scheme, thus providing a relatively compact layout minimizing the electron beam energy and total footprint.

It was mentioned above that a diversity of applications can be found in very different research fields, see for example [8] and references therein. Specific case studies can be identified, for example, on the basis of the energy content of the scattered light. At low photon energy (up to few MeV), contrast imaging of massive objects in Geo-archeology [7] would greatly benefit from such an intense and compact source, and this was actually the driving case of this work. At photon energies in the 1–10 MeV range, photons propagating though dense materials prompt nuclear reactions, generating e.g. alpha particles and neutrons, which can be easily identified and used for separating isotopes [9]. At photon energies higher than 10 MeV, the proposed scheme would approach the specifications for an elastic photon-photon scattering source for frontier experiments in QED [10]. Even if all these examples were equivalently considered in the presence of an external laser, it is undoubtedly demonstrated below that a higher electron beam energy would be required at the interaction point, for the same output photon energy, and therefore a longer, more expensive electron linear accelerator. Moreover, as a by-product of the proposed scheme, a naturally synchronized UV beam with large fraction of coherent photons, and at 100 fs duration level would be provided by the FEL, which is ideal for pump-probe experiments. High-flux Multi-MeV gamma-ray beams and UV radiation can be simultaneously available for applications in Nuclear Physics, Security Inspections, Cultural Heritage and UV Science.

* Soil blocks resulting from archaeological excavations may contain different kinds of artifacts of interest in cultural heritage.

## 2. X-Ray Attenuation

The efficiency of transmission imaging techniques like radiography and tomography depends on the attenuation processes occurring in the radiation-matter interaction. The Beer-Lambert law [11] characterizes the interaction of X-rays with matter through a transmission function involving the cross section of physical processes like photoelectric absorption, Compton scattering and pair production. Using the absorption coefficients in [12] we evaluated (Table 1) the transmission, $\Gamma(\mu)$, of 20 MeV gamma-rays in10 cm thick samples of different materials. For most materials of interest the transmission is large.

**Table 1.** Transmission of 20-MeV gamma-rays through a thickness $\tau$=10-cm of different materials.

| **Sample** | **Z** | **$\rho$ [g/cm$^3$]** | **$\mu$ [10$^{-2}$ cm$^2$/g]** | **$\Gamma(\mu)$ [%]** |
|---|---|---|---|---|
| Al | 13 | 2.72 | 2.17 | 55.4 |
| Fe | 26 | 7.87 | 3.22 | 8.0 |
| Cu | 29 | 8.96 | 3.41 | 4.7 |
| Ag | 47 | 10.49 | 4.61 | 0.79 |
| Au | 79 | 19.32 | 6.14 | $7.1\times10^{-4}$ |
| Pb | 82 | 11.35 | 6.21 | $8.7\times10^{-4}$ |
| Bone | - | 1.92 | 2.07 | 67.2 |
| Concrete | - | 2.30 | 3.44 | 45.3 |
| Calcite | - | 2.71 | 2.28 | 53.9 |

## 3. The FEL-ICS Scheme

In a classical ICS process a relativistic electron transfers a fraction of its energy to an incoming laser photon which is scattered in the electron direction of flight with a Doppler-upshifted frequency. The scattered radiation energy

$$E_s = \frac{a_C}{1+X}\gamma^2\hbar\omega_{ph} \tag{1}$$

exhibits a quadratic energy dependence on the electron energy as the incoming photon energy $\hbar\omega_{ph} = E_L$ is constant. The kinematic factor

$$a_c \approx \frac{2(1+\cos\varphi)}{1+(\gamma\theta)^2} \le 4 \tag{2}$$

modulates the scattered energy via the collision angle $\varphi$ within the semi-aperture $\theta$ of the emission cone, while the term

$$X = 4\gamma\frac{\hbar\omega_{ph}}{m_e} \tag{3}$$

accounts for the recoil of the electron [13]. Its contribution introduces a red-shift in the spectra of the emitted radiation (1) and can have not negligible effects in terms of required radiation bandwidth [14].

The FEL-ICS scheme introduces a stronger $\gamma$-dependence by making the relativistic electron beam interact with its own UV radiation produced in an FEL [15].
The on-axis FEL radiation wavelength is related to the axial electron velocity $\beta_z$ and the undulator period $\lambda_u$ as [16]:

$$\lambda_r = \lambda_u \frac{1-\beta_z}{\beta_z} \approx \frac{\lambda_u}{2\gamma^2}(1+a_u^2) \quad . \tag{4}$$

Here $a_u = K_u = eB_0\lambda_u/2\pi m_e c = 93.4 B_0[T]\lambda_u[m]$ is the helical undulator parameter

($a_u = K_u/\sqrt{2}$ for a planar-polarized undulator), $B_0$ the undulator central magnetic field, $e$ the electron charge. The energy of the FEL photons in terms of the electron energy reads:

$$E_r \propto \frac{hc}{\lambda_r} = a_{FEL} hc \frac{\gamma^2}{\lambda_u} \tag{5}$$

where we define $a_{FEL} = 2/(1+a_u^2)$ for on axis undulator radiation.

When the FEL photon energy (5) replaces that from the laser in Eq.1, i.e., $\hbar\omega_{ph} = E_r$, the scattered photon energy can be written as:

$$E_s = a_C E_r \gamma^2 = a_C a_{FEL} hc \frac{\gamma^4}{\lambda_u} \quad . \tag{1'}$$

In this kinematic scaling the term (3), of the order of $5.5 \times 10^{-2}$ with the parameter list of Table 4, has been neglected.

Introducing the Compton wavelength $\lambda_c = hc/m_e c^2 = 2.426 \times 10^{-3}$ nm the scattering efficiency, i.e the fraction of the electron energy transferred to the scattered photons, reads

$$\eta \propto \frac{E_s}{E} = a_C a_{FEL} \frac{\lambda_c}{\lambda_u} \gamma^3 . \tag{6}$$

While the scattering efficiency in the ICS case scales linearly with beam energy, the cubic energy dependence in Eq. 6 provides compactness to the system, as lower electron energy is required to produce a given upshifted radiation. Additional flexibility in the UV energy and thus in the FEL-ICS radiation is available as they are tunable via the undulator parameter $K_u$, typically ranging from 1 to 5 in an out-of-vacuum APPLE-II type device [17] or Delta undulator [18].

The collision angle $\varphi$, ideally null in classical ICS schemes, is in our case different from zero to allow room for optical components at the IP. Its choice results from the optimization of different competing requirements, like the scattering efficiency, via the impact parameter $a_C$ (Eq. 2), the ICS luminosity and the extension of the loop in Fig. 2, both accounted for in section 4. As a result, a conservative interaction angle $\varphi = 25^0$ has been assumed in the FEL-ICS baseline design.
The dependence of the incoming (5) and scattered photon energy (1') on the electron beam energy is shown in Fig.1.

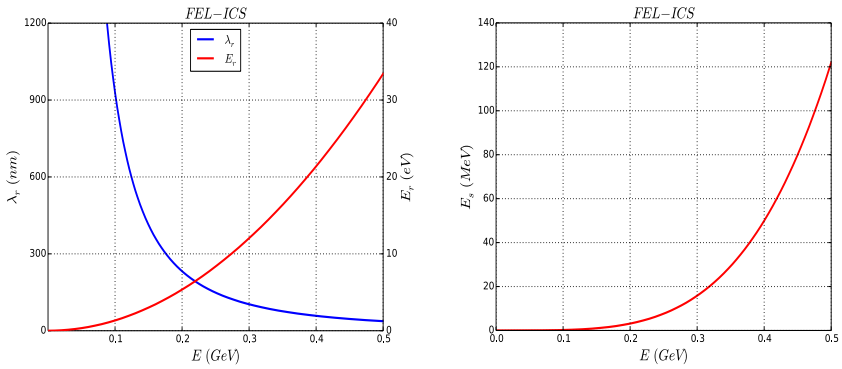


**Fig. 1.** FEL-ICS: scattered radiation energy (left), wavelength of the incoming radiation from undulator with $\lambda_u$=20 mm (center), and scattering efficiency.

A numerical evaluation of the scattered (Eq.1') and ingoing (Eq.5) photon energies together with the efficiency (Eq.6) is collected in Table 2 for five values of the electron energy and a conservative set of parameters $l_u = 20\,mm, j = 25^0$.

**Table 2.** FEL-ICS: Incoming (UV) and scattered photon energy and scattering efficiency as a function of the electron energy.

| $E$ [MeV] | $E_r$ [eV] | $\lambda_r$ [nm] | $E_s$ [MeV] | $\eta = E_s/E$ |
|---|---|---|---|---|
| 100 | 1.3 | 928.1 | 0.2 | $2.0\times10^{-3}$ |
| 200 | 5.3 | 232.0 | 3.1 | $1.6\times10^{-2}$ |
| 300 | 12.0 | 103.2 | 15.8 | $5.3\times10^{-2}$ |
| 400 | 21.4 | 58.0 | 50.0 | $12.5\times10^{-2}$ |
| 500 | 33.4 | 37.1 | 121.9 | $24.4\times10^{-2}$ |

It can be gathered from the FEL-ICS figures in Table 2 that:

i. The ~16 MeV outgoing radiation energy for the 300 MeV electron energy considered in the present study compares with the ~3 MeV obtainable in the classical ICS case.

ii. The scattering efficiencies $E_s/E$ are larger than in the ICS case by one order of magnitude or more in the present energy range, and the comparison dramatically improves with the electron energy.

iii. The incoming photon energies $E_r$ are still a small fraction of the electron rest mass even in the reference frame of the electron beam, justifying the use of the Thomson classical cross section in the evaluation of the scattered radiation fluxes neglecting the recoil term (3).

## 4. A Baseline FEL-ICS System and its Components

### *4.1 Description of the baseline scheme*

A single-pass conceptual layout providing a strong source of multi-MeV photons is shown in Fig. 1. The main characteristics of the system are summarized in Table 2 and discussed in the following sections. Trains of electron bunches from an X-Band Linac are focused at the IP where they collide with FEL radiation produced by earlier bunches. A return arc guides the electrons into an FEL undulator. The return arc is designed to act as a bunch length compressor [19,20], raising the electron bunch peak current from 35 A to 500 A for an improved FEL performance. The FEL operates in the high-gain SASE regime [16,21] and is long enough to reach saturation. The emerging UV radiation is focused at the IP, where high-energy gamma-rays are produced via Compton interaction with the trailing bunches. The $180^0$ original arc deflection in Ref. [19] is extended to $205^0$ to produce collisions at the $25^0$ design interaction angle. The low value of the Thomson cross section preserves the electron bunch quality for the FEL and allows subsequent use of the UV radiation for additional applications.

The large FEL power compensates for the low Thomson cross-section. The electron bunches and UV radiation are focused to similar transverse spot sizes at the IP to optimize the scattered flux. The electron focusing, bunch compression, and UV optics are all crucial for providing the desired compactness and gamma-ray flux. The short undulator length allowed by bunch compression, an arc compressor length of about 6.5 m and the associated matching optics leave about 2 m for the UV focusing drift downstream the undulator.

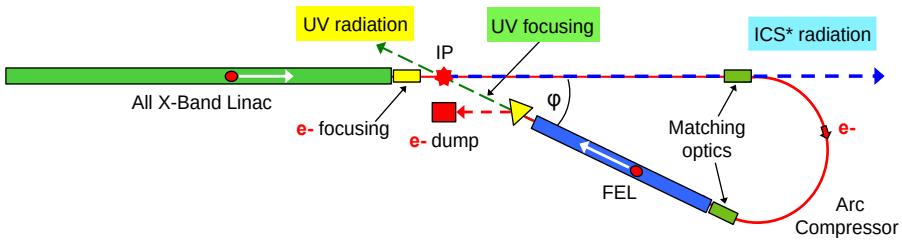


**Fig. 2**. The FEL-ICS single-pass scheme involving a return arc and an FEL. The return arc provides longitudinal compression to the electron bunches for improved FEL performance. UV radiation and electron bunch focusing at the IP provide overlap control and optimize the ICS Luminosity. Two photon energies are simultaneously available to experiments, UV radiation in the 15–20 eV range, and gamma-rays in the 10-20 MeV range. The system footprint is about 4x21 $m^2$.

Other FEL-based ICS schemes, using an optical cavity to generate collisions between the FEL photons and the electron beam, exist [6] or have been proposed [22]. Our scheme removes this requirement and is not limited to FEL wavelengths for which highly reflective mirrors at normal incidence are available, taking full advantage of the scaling law of Eq. 1'. The main characteristics of the system are summarized in Table 3 and discussed in the next sections.

### *4.2 The Linear Accelerating Structure*

We consider a room temperature operation in the original spirit of keeping the photon source within cost-effective limits. Compactness requirements suggest the adoption of high-gradient X-Band technology [23], both for the photo-injector and the accelerating structure. Power dissipation issues associated to the acceleration of electron beams with kilohertz time structures can be mitigated by choosing operating frequencies in the 11.4–12.0 GHz range in order to increase the RF power transfer efficiency with a higher specific shunt impedance of the structure, proportional to its frequency [24]. Warm X-Band RF technology operating at the above-mentioned repetition rates with a 35 MV/m gradient, considerably lower than the 100 MV/m reached at the CTF [25] *in laboratory operating conditions*, has been considered in [26] and is adopted in this design.

An X-Band photo-injector has been built and commissioned at the X-Band Test Area (XTA) at SLAC [27] with good beam quality. Complementing this injector with a 9 m long, 35 MV/m X-Band accelerating structure sets up an "all X-Band Linac" [27] capable of delivering a 300 MeV electron beam within a ~10 m total length. The 1 kHz repetition rate of the ~1 μs long RF pulse containing 100 electron bunches gives an average beam current of about 30 μA and a 9 kW beam power to the dump.

Operation of the X-band linac at the high gradient of 100 MV/m can only be envisioned at a repetition rate lower than 100 Hz, and in single pulse mode. This scenario would therefore shrink the linac length to approximately 3 m for a final beam energy of 300 MeV. However, the average electron beam current, as well as the average FEL-ICS photon flux would be lowered by a factor 1000 with respect to the low-gradient, high pulse rate option, which therefore remains our basic design.

**Table 3.** Baseline parameter list for the FEL-ICS with return arc compressor.

| **SYSTEM** | **Value** | **Unit** |
|---|---|---|
| **Linac** | | |
| Electron Beam Energy | 300 | MeV |
| Photo-Injector RF Frequency (X-Band) | 11.4-12.0 | GHz |
| Linac RF Frequency (X-Band) | 11.4-12.0 | GHz |
| Linac Accelerating Gradient | 35 | MV/m |
| Linac Length | ~9 | m |
| Bunch Charge | 300 | pC |
| Initial Bunch Duration, rms | 2.5 | ps |
| Initial Bunch Peak Current | 35 | A |
| Initial Normalized Emittance (x,y), rms | 0.7, 0.7 | mm mrad |
| Train Repetition Rate | 1 | kHz |
| Number of Bunches per Train | 100 | |
| Average Beam Current | 30 | μA |
| Beam Power to Dump | 9 | kW |
| **Return Arc Compressor** | | |
| Magnetic Cell Type | DBA-like | |
| Arc Length | 6.5 | m |
| Central trajectory average radius | 1.82 | m |
| Compression Factor | 15 | |
| Final Peak Current | 500 | A |

| | | |
|---|---|---|
| Final Normalized Projected Emittance (x,y), rms | 1.0, 1.0 | mm mrad |
| Final Correlated Relative Energy Spread | 0.2 | % |
| Final Uncorrelated Relative Energy Spread | 0.02 | % |
| **Free Electron Laser** | | |
| Undulator Magnetic Structure | Helical | |
| Undulator Peak Field | 0.86 | T |
| Undulator Period Length | 20 | mm |
| Undulator Total Length | ~5 | m |
| Undulator Parameter | 1.6 | |
| FEL Wavelength | 103 | nm |
| FEL Parameter | $5.5\times10^{-3}$ | |
| FEL Gain Length | 0.22 | m |
| FEL Peak Saturation Power | 0.77 | GW |
| UV Peak Flux | $4\times10^{26}$ | photons/s |
| FEL Duty Factor | $6\times10^{-8}$ | |
| UV Average Power | 46 | W |
| UV Average Flux | $2\times10^{19}$ | photons/s |
| UV Focusing Drift | 2.5 | m |
| UV Coherent Angle | 0.16 | mrad |
| UV Coherent Radius | 0.052 | mm |
| **System footprint** | ~4x21 | $m^2$ |

### *4.3 The return Arc Compressor*

The electron bunch peak current drives the FEL output peak power so electron bunch length compression is critical for the flux of UV FEL photons interacting at the interaction point (IP). The return arc compressor in Fig.2 gives a 205° beam deflection via a modified double-bend achromatic cell magnetic structure characterized by a 3.58 Tm integrated bending field at $E$=300 MeV. The 6.5 m central arc trajectory length yields a bunch length compression factor C≈15 for 300 pC bunches, while limiting the growth of the transverse projected normalized emittances – here weakly affected by the emission of coherent synchrotron radiation (CSR) – to about 0.3 μm.

The outgoing bunch has 0.5 kA peak current, 1 $\mu$m normalized projected emittances and ~0.2% correlated rms energy and energy distribution. Nevertheless, the final relative slice energy spread remains about one order of magnitude lower than the spread. Particle tracking indicates that CSR emission in the arc dipoles leads to some modulation in the bunch current profile FEL parameter threshold, and no relevant impact on the FEL performance is anticipated.

The bunch final peak current of 0.5 kA is important to obtain high average FEL photon flux and reduce the undulator gain length.

### *4.4 The UV FEL*

After bunch length compression the beam is injected into the undulator. In the 1-D approximation the FEL gain length is given in terms of the 'FEL parameter' $r_{FEL}$ [21] by

$$L_G = \frac{l_u}{4p\sqrt{3}r_{FEL}} \cdot \quad (7)$$

The radiation bandwidth and the saturation power to electron beam power ratio scale linearly with the FEL parameter.

In the scenario depicted in Fig.2 a helical undulator is proposed to maximize the output power of the UV FEL, reduce the gain length and provide transverse focusing. A compact design based on Permanent Magnet technology [17,28] can provide the desired field amplitude, such as $B_0$=0.86 T at $\lambda_u$=20 mm, and eventually an undulator parameter $a_u$=1.60. A ~5 m long undulator allows the FEL to reach saturation at the fundamental wavelength of 103 nm (12 eV photon energy). The analytical evaluation of the undulator length needed to reach saturation is shown in Fig. 3 as a function of the beam peak current, along with the final average gamma-ray photon flux. With the undulator and electron beam parameters collected in Table 3 the FEL parameter is about $5.5\times10^{-3}$, the gain length 0.22 m and the FEL peak power at saturation 0.77 GW. The corresponding photon peak rate is $4\times10^{26}$ UV ph/s.

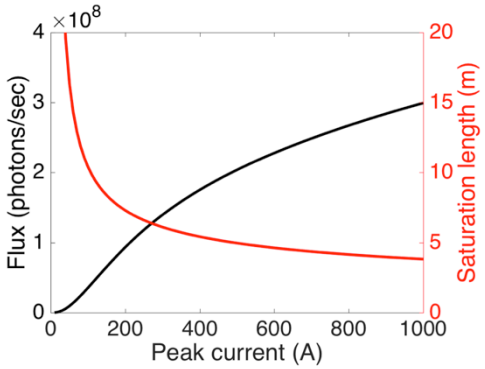


**Fig. 3.** FEL-ICS performance in terms of scattered photon flux and FEL saturation length vs. the electron bunch peak current, for an undulator period length $\lambda_u$=20 mm.

### *4.5 Beam Focusing and Tuning*

Electron beam and UV focusing at the IP are crucial ingredients for the optimization of the ICS luminosity by matching the rms size of the electron and photon beams at the IP. The UV optical focusing system uses a single toroidal mirror operating at grazing incidence [29] to compensate the FEL photon beam divergence and produce a 15 μm vertical, 60 μm horizontal photon sizes at the IP, via a demagnification factor of about 4 in the vertical plane and 1 in the horizontal plane for the photon beam dimension at the undulator exit (Table 3). A bare silicon surface has ~97% reflectivity at 103 nm and 2° grazing incidence.

A quadrupole triplet at the end of the linac controls the electron beam sizes to match those of the UV beam.

The matching of the electron and photon transverse beam sizes increases the scattered photon flux by over an order of magnitude compared to a case with no UV focusing.

The pointing stability of the FEL output pulse, associated to the above mentioned photon demagnification, is a point of concern. A tolerance on the shot-to-shot variation of the FEL pulse position of the order of 1/5 of the rms size requires the FEL trajectory to be controlled at the level of ~10 μm in both planes. For a minimum betatron function of approximately 2.5 m along the undulator, the control of the electron beam angular divergence has to be at the level of ~10 μm /2.5 m = 4 μrad. State-of-the-art SASE FELs in single pass facilities feature a < 5 μm, < 1 μrad rms electron trajectory jitter by adopting < 2 μm resolution RF cavity beam position monitors [30]. The unavoidable residual jitter is typically dominated by RF jitter sources in the accelerator that, for the aforementioned ranges of fluctuations, stay at the rms level of 0.1% for the peak voltage, and to $0.1^0$ (from S-band to X-band) for the phase [31]. In summary, the proposed FEL-ICS scheme requires a good beam control largely feasible with the presently available technology.

### *4.6 – Electron Beam Dump*

The 9 kW average electron beam power is spent in a dump (Fig.2). The electron beam transverse dimensions at this location are larger than 0.1 mm rms in both planes and the single pulse energy density is less than 0.17 J/mm$^2$/pulse. A 0.5 m long cylindrical dump, made of an inner core of Graphite surrounded by Aluminum, would ensure >99% energy absorption efficiency with negligible production of isotopes.

## 5. Beam Temporal Structures and Event Rate

The beam temporal structure consists of bunch trains of length $\tau_t$ repeating at the RF pulse rate $k_t$. Each train contains $k_b$ bunches with a time separation

$$t_b = t_t / k_b \circ m t_G \tag{8}$$

multiple of the gun bucket separation $\tau_G$.

The leading bunches in each train do not contribute to the ICS process as they need to fill the loop of Fig.2 before radiating in the undulator and initiate the scattering process. If $k_{loop}$ is the number of bunches uniformly filling the loop length $L_{loop}=c\,\tau_{loop}$, we have with the definition in Eq.8:

$$k_{loop} = L_{loop} / c\, t_b = k_b\, t_{loop} / t_t \tag{9}$$

and the number of bunches in each train actually interacting in the FEL-ICS scheme is:

$$k_{bx} = k_b - k_{loop} = k_b (1 - t_{loop} / t_t) \quad . \tag{10}$$

Adopting Eq.10 the event rate (photons per second) for the FEL-ICS process is

$$\dot{N}_{ph}^{ICS} = \frac{\sigma_T}{e\, A(\varphi)} I_L\, N_{ph}^{U} (1 - \tau_{loop} / \tau_t) \tag{11}$$

Here $\sigma_T$ = 0.665 barn is the Thomson cross section, $I_L=k_t\ k_b\ q_b$ the average Linac current and $N_{ph}^U$ the number of photons per FEL pulse. The interaction area $A(\varphi)$ for Gaussian bunches colliding at an angle $\varphi$ in the horizontal plane

$$A(j) = 2p\mathsf{S}_y\sqrt{\mathsf{S}_x^2+\mathsf{S}_z^2\tan^2(j/2)} \qquad (12)$$

involves, in the general case of non-equal bunches, the convoluted transverse bunch sizes $\mathsf{S}_s = \sqrt{s_{s1}^2+s_{s2}^2}\ \ (s=x,y,z)$, which can be optimized as discussed above.

The evaluation of the event rate (11) in Table 4 takes into account the different longitudinal dimensions of the colliding bunches. While the UV FEL pulse in the SASE regime has an rms duration comparable to that of the electron bunch after compression, approximately 0.16 ps, the electron bunch at the IP is still uncompressed and has a parabolic current profile with an rms duration of 2.5 ps.

For a given value $\bar{R}_{ARC}$ of the average radius of the central trajectory in the return Arc the interaction angle $\varphi$ defines the loop extension

$$L_{loop} \gg \bar{R}_{ARC}\left(p+j+\frac{2}{\tan j/2}\right). \qquad (13)$$

Given the synchronism condition between the loop length and the bucket separation (8)

$$t_{loop} \circ \frac{L_{loop}}{c} = k_b\, t_b \qquad (14)$$

the loop length (13) assumes discrete values and involves appropriate choices for the set $\{j, \bar{R}_{ARC}\}$.

With the electron beam and undulator parameters listed in Table 3 the system geometry of Fig.2 deals with 90 interacting electron bunches per train (Eq.10) and the interaction rate at the IP is 90 kHz. The characteristics of the photon and electron colliding beams, and of the scattered gamma-rays are summarized in Table 4. The average gamma-ray photon flux and the undulator saturation length are shown as a function of the beam peak current in Fig. 3. At our 500 A design value we have $1.1\text{x}10^8$ ph/s and 5.0 m respectively. The ideal minimum bandwidth for the gamma-rays is 0.9%, determined by a combination of the projected energy spread of the electron bunch, the SASE FEL bandwidth and the angular spread of the electrons. The average scattered photon energy is half of the maximum photon energy, and the scattered intensity on axis is taken to be the total flux divided by a solid angle of $2\pi/3\gamma^2$ [32].

## 6. System Footprint

The short undulator length allowed by bunch compression makes the width of the footprint of the single-pass scheme in Fig.2 essentially determined by the Linac length and the return loop width:

$$W_{fp} \sim L_{LINAC} + W_{loop} \tag{15}$$

with

$$W_{loop} \sim \bar{R}_{ARC}\left(1 + \frac{1}{\tan\varphi/2}\right) \tag{16}$$

The choice of the interaction angle is the result of a compromise between Luminosity optimization and loop extension. Reducing the crossing angle to maximize the ICS Luminosity (11,12) would increase the loop width (16) and the system footprint.
With the parameters of Table 3 the linac structure is ~9 m long and the system footprint is ~4x21 $m^2$.

**Table 4.** Beam parameter list at the Interaction Point.

| **Parameter** | **Value** | **Unit** |
|---|---|---|
| Electron Beam Energy | 300 | MeV |
| Bunch Charge | 300 | pC |
| Bunch Duration, rms | 2.5 | ps |
| Bunch Peak Current | 35 | A |
| UV Photon Energy | 12.0 | eV |
| UV Peak Flux | $2\times10^{19}$ | photons/s |
| UV Duration, rms | 0.16 | ps |
| UV and e- rms beam sizes at IP (x / y) | 60 / 15 | μm |
| Interaction Angle | 25 | deg |
| Interacting e- Bunches per Train | 90 | |
| Interaction Rate | 90 | kHz |
| ICS Duty Factor | $7.7\times10^{-7}$ | |
| Scattered Photon Maximum Energy | ~16 | MeV |
| Scattered Photon Average Flux | $1.1\times10^{8}$ | photons/s |
| Scattered Photon Average Power | 0.14 | mW |
| Scattered Photon Average Intensity | $1.8\times10^{7}$ | photons/s/$mrad^2$ |
| Scattered Photon Peak Flux | $1.4\times10^{14}$ | photons/s |
| Scattered Photon Peak Power | $1.8\text{x}10^{5}$ | mW |
| Scattered Photon Peak Intensity | $2.3\times10^{13}$ | photons/s/$mrad^2$ |

## 7. Upgrade Options

A higher average photon flux is certainly appreciated in experiments that rely on statistics [33] such as those cited in the Introduction as case studies as well as experiments implementing ultrafast dynamics and spectroscopy for the physics of matter at molecular scale. The average photon flux can be made larger at the expense of increasing the complexity of the device, in particular by requiring cryogenic cooling. Superconducting L-

Band accelerating structures with frequencies of 1.3 or 1.5 GHz, have been designed for multiple accelerator facilities. Peak gradients are comparable to that of S-Band structures, in the range of 10-20 MV/m, and with quality factor $Q > 10^{10}$ may be run in CW mode. A single 8 m cryomodule can yield a ~120 MeV energy gain.

The LCLS-II design [34] has a nominal average current of 20 μA, with a technical limit of 300 μA. With no beam slowing or energy recovery, the main constraint is on the beam dump, which for a 4 GeV beam would need to accept up to 1.2 MW.

For a 300 MeV beam energy, a 500 kW beam power at the beam dump would allow an average Linac current of 1.7 mA, corresponding to an increase by a factor ~50 in the total photon flux compared to that evaluated at room temperature operation. The use of energy recovery, such as at the Cornell ERL [35], could allow 100 mA average current but requires a large R&D effort in cavity design and feedback systems. However, significantly more than 1 mA may be achievable using already engineered systems.

The benefits of using SC undulators are not as dramatic as those of SC acceleration. However, by allowing a higher undulator parameter at shorter periods, SC undulators can be used to reduce the beam energy, increase the scattered photon energy, and/or reducing the undulator length. Any improvement in the photon flux will be modest at best.

Finally, seeding the FEL process would improve stability and shorten the required undulator length. It could be achieved either with an external source or through regenerative amplification [36] by sending a small fraction of the output FEL radiation back into the undulator. However, a further reduction of the undulator length would add limited compactness to the system footprint, mainly determined by the return arc length.

## 7. Summary

Nearly monochromatic multi-MeV gamma-ray beams can find applications in the Industry and Defense fields where their characteristics can play an important role in the analysis of materials and in the detection of illegal specimens. In the Geoarchaeology and cultural heritage fields, X-ray Computed Tomography (XCT) techniques [4,6], presently adopted for the visualization and analysis of archaeological artifacts contained in soil blocks of limited dimensions (~0.05 $m^3$), can benefit from the availability of gamma-ray beams in the tens of MeV range to extend the present fields of application.

By interacting with its own FEL radiation through an Inverse Compton Scattering process, a relatively low energy electron beam can simultaneously produce UV photons in the 10 to 12 eV range, and high-energy gamma-rays in the 6-16 MeV range. These photon beams can be used for Cultural Heritage, Nuclear Physics and UV science.

A compact ~5 m long undulator is sufficient to simultaneously produce an UV flux of ~$2x10^{19}$ ph/s and a high-energy photon flux in excess of $2x10^8$ ph/s, within a system footprint of about 4x21 $m^2$. The scheme can be considered as an alternative to neutrons for the analysis of soil blocks of a certain volume containing archaeological findings like prehistoric teeth and old jewelry in the Geoarchaeology and Cultural Asset field. Moreover, it offers options for a wide range of multi-MeV photons applications in the Industry and Defense environments. Ideas to increase the photon flux seem feasible at the expense of increasing the complexity of the device, in particular by requiring cryogenic cooling.

In a classic ICS setup, where the incoming electron beam interacts with the electromagnetic field of a laser, the energy of the emitted radiation scales with the square of the electron energy. In the proposed FEL-ICS setup the scattering field is provided by

the photon beam radiated in an undulator by the electron beam itself. For a given outgoing radiation energy the footprint of the setup becomes *much more compact* since the energy of the emitted radiation scales with the fourth power of the electron energy. As an example, gamma-rays in the 16 MeV range can be produced with a ~300 MeV electron beam as compared to the ~700 MeV required in a conventional ICS system. Tunability is provided via the undulator parameter. The characteristics of the incident photon flux from the undulator, its gain length and the associated overall compactness of the setup strongly depend on the peak current of the electron bunches.

The 500 A bunch peak currents attainable with the adoption of the arc compressorscheme for the electron return arc, provide a setup footprint of ~4x21 $m^2$, about a factor of four smaller than the one achievable without bunch compression. Seeding options in the FEL process can furthermore reduce the length of the undulator. However, the system footprint remains determined by the return arc length.

Superconducting L-Band accelerating structures with peak gradients of 10 to 20 MV/m can increase by a factor of 50 the average Linac current and the outgoing radiation flux. The beam power to the dump sets technical limitations. The benefits of using SC undulators are not as dramatic as those of SC acceleration. However, by allowing a higher undulator parameter at shorter periods, some combination of improvements can be achieved, like reducing the required beam energy, increasing the radiated photon energy or reducing the undulator length.

## Acknowledgements

One of the authors (MP) wishes to acknowledge the possibility of sharing the interest for high-energy photon sources devoted to analysis, characterization and preservation of Cultural Heritage with F. Casali and F. Boscherini (Bologna University). Valuable contributions from G. D'Auria, L. Doolittle and F. Sannibale on Linac technical aspects are acknowledged and from D. Cocco for a feasibility estimate of a UV focusing system. We also thank A. Ratti for encouraging and supporting this study. This publication was funded by the Accelerators Group of Elettra Sincrotrone Trieste and by the Director, Office of Science, of the U.S. Department of Energy under Contract No. DE-AC02-05CH1123.

## References

[1] A. Olivo and E. Castelli, "*X-ray phase contrast imaging: From synchrotrons to conventional sources*", Rivista del Nuovo Cimento, DOI 10-1393/ncr/i2014-10104-8, Vol. 3, N. 9, June 16, 2014.

[2] K. Yamada *et al., "A trial for fine and low-dose imaging of biological specimens using quasi-monochromatic laser-Compton X-rays",* NIM-A 608 (2009) S7-S10.

[3] J. Stelzner *et al., "The application of 3D computed tomography with X-rays and neutrons to visualize archaeological objects in blocks of soil"*, STUDIES IN CONSERVATION 55 (2010), 95-106.

[4] F. Casali, "*X-ray and neutron digital radiography and computed tomography for cultural heritage*", Physical Techniques in the Study of Art, Archaeology and Cultural Heritage, Volume I, ed. D. Bradley and D. Creagh, Elsevier, Amsterdam (2006) 41-123.

[5] A. Re *et al.*, "*X-ray tomography of a soil block: a useful tool for the restoration of archaeological finds",* Heritage Science 2015, 3:4 (3 February 2015) doi:10.1186/s40494-015-0033-6. http://www.heritagesciencejournal.com/content/3/1/4.

[6] E. Esarey, S. K. Ride and Ph. Sprangle, "*Non linear Thomson scattering for Intense laser pulses from beams and plasmas*", Phys. Review E, Vol. 48-4, Oct. 1993.

[7] F. Casali *et al, "X-ray computed tomography for damage assessment of cultural heritage assets",* Protection of Historical Buildings, PROHITECH 09, Mazzolani (ed), 2009 Taylor & Francis Group, London, ISBN 978-0-415-55803-7.

[8] G. Sarri *et al., "Ultrahigh Brilliance Multi-MeV $\gamma$-Ray Beams from Nonlinear Relativistic Thomson Scattering",* PRL 113, 224801 (2014), doi: 10.1103/PhysRevLett.113.224801.

[9] C. P. J. Barty, "*Nuclear photonics with laser-based gamma rays*", *SPIE Opt. Optoelectron*. Paper 8080B-30 (2011), doi: 10. 1117/2. 1201110.003681.

[10] D. Micieli *et al.*, PRST-AB 19, 093401 (2016).

[11] A. Beer "*Bestimmung der Absorption des rothen Lichts in farbigen Flüssigkeiten*" (Determination of the absorption of red light in colored liquids), *Annalen der Physik und Chemie*, vol. 162, pp. 78–88, (1852), doi:10.1002/and p.18521620505.

[12] S. M. Seltzer, "*Calculation of Photon Mass Energy-Transfer and Mass Energy-Absorption Coefficients*", Radiation Research 136 (1993) 147-170; cf. Table 4 of NIST data at https://www.nist.gov/pml/x-ray-mass-attenuation-coefficients and online absorption calculator at http://webdocs.gsi.de/~stoe_exp/web_programs/x_ray_absorption/index.php.

[13] A. Curatolo *et al., "Analytical description of photon beam phase spaces in Inverse Compton Scattering sources",* arXiv:1705.07740v1 [physics.acc-ph], 22 May 2017.

[14] L. Serafini, *private communication.*

[15] H. Motz, W. Thon and R.N. Whitehurst, "*Experiments on Radiation by Fast Electron Beams*", J. *Appl. Phys.* **24**, No. 7, (1953) 826, doi:10.1063/1.1721389.

[16] C. Pellegrini, A. Marinelli and S. Reiche, "*The physics of free-electron lasers*", Reviews of Modern Physics **88** (2016) 015006, doi:10.1103/RevModPhys.88.015006.

[17] A. B. Temnykh, "*Delta undulator for Cornell energy recovery linac*", Phys. Rev. ST Accel. Beams 11 (2008) 120702, doi:10.1103/PhysRevSTAB.11.120702.

[18] S. Sasaki, "*Analyses for a planar variably-polarizing undulator*", Nucl. Instr. Meth. A **347** (1994) 83-86, doi:10.1016/0168-9002(94)91859-7.

[19] S. Di Mitri and M. Cornacchia, "*Transverse emittance-preserving arc compressor for high-brightness electron beam-based light sources and colliders",* EPL **109** (2015) 62002, doi:10.1209/0295-5075/109/62002.

[20] S. Di Mitri, "*Feasibility study of a periodic arc compressor in the presence of coherent synchrotron radiation"* Nucl. Instr. Meth. A 806 (2015) 184-192, doi:10.1016/j.nima.2015.10.015.

[21] R. Bonifacio, C. Pellegrini and L. M. Narducci, "*Collective instabilities and high-gain regime in a free electron laser*", Opt. Commun. **50** (1984) 373, doi:10.1016/0030-4018(84)90105-6.

[22] B. E. Carlsten *et al*., "*High repetition-rate inverse Compton scattering x-ray source driven by a free- electron laser*", J. Phys. B 47 (2014) 234012, doi:10.1088/0953-4075/47/23/234012.
[23] G. D'Auria, "*Application of X-Band Linacs",* Proc. LINAC2012, Tel-Aviv, Israel (2012) 724-728, ISBN 978-3-95450-122-9.
[24] C. Christou, "*X-band linac technology for a high repetition rate light source*", Nucl. Instr. Meth. A **657** (2011) 13, doi:10.1016/j.nima.2011.06.050.
[25] W. Wuensch, HG2012 Workshop, 18-20 April 2012, KEK, Tsukuba, Japan.
[26] R. Bartolini, "*Beam dynamics optimisation of an X-band Linac driven soft X-ray FEL*", Nucl. Instr. Meth. A **657** (2011) 177, doi:10.1016/j.nima.2011.06.046.
[27] C. Limborg-Deprey *et al., "Achieved Performance of an All X-Band Photo-Injector*", Proc. IPAC2016, Busan, Korea. (2016) 4253, ISBN 978-3-95450-147-2.
[28] H.-D. Nuhn *et al*., "*Commissioning of the Delta Polarizing Undulator at LCLS*", Proc. FEL2015, Daejeon, Korea (2015) 757-763, ISBN 978-3-95450-134-2.
[29] D. Cocco, *private communication*.
[30] P. Frisch *et al.,* in Proc. of Intern. FEL Conf., THB04, Basel, Switzerland (2014).
[31] P. Craievich *et al*. PRST-AB 16, 090401 (2013).
[32] D. Fargion, R.V. Konoplich and A. Salis, "*Inverse compton scattering on laser beam and monochromatic isotropic radiation*", Z. Phys. C **74** (1997) 571—576, doi:10.1007/s002880050420.
[33] W. Graves, "*Compact x-ray source based on burst-mode inverse Compton scattering at 100 kHz*", PRST-AB **17, 120701 (2014)**].
[34] LCLS-II Design Study Group, "*LCLS-II conceptual design report*", Report LCLSII-1.1-DR-0001-R0, SLAC, January 2014.
[35] M. Liepe, D. Hartill, G. Hoffstaetter, S. Posen, and V. Veshcherevich, "*Experience with the Cornell ERL injector srf cryomodule during high beam current operation*", Proc. IPAC2011, San Sebastian, Spain, (2011) 35-37.
[36] D. C. Nguyen *et al.,* "*First lasing of the regenerative amplfier FEL*", Nucl. Instr. Meth. A **429** (1999) 125-130, doi:10.1016/S0168-9002(99)00090.